# Thermoelastic and Optical Properties of Thick Boride Templates on Silicon for Nitride Integration Applications

R. Roucka,[†] V. R. D'Costa,[‡] Y.-J. An,[†] M. Canonico,[§] J. Kouvetakis,[†] J. Menéndez,[‡] and A. V. G. Chizmeshya*,[†]

*Department of Chemistry and Biochemistry, Arizona State University, Tempe, Arizona 85287; Department of Physics, Arizona State University, Tempe, Arizona 85287; and Freescale Semiconductor, Tempe, Arizona 85284*

*Received September 6, 2007. Revised Manuscript Received November 19, 2007*

We present a comparative study of the structural, thermoelastic, and optical properties of $ZrB_2$ films grown on silicon with the corresponding bulk $ZrB_2$ behavior. Thick $ZrB_2$ films (up to 500 nm) with device quality morphological and structural properties were grown on Si(111) for potential integration of GaN with Si substrates. HR-XRD was used to analyze the thickness and temperature dependence of the films' strain state. The data indicate that at room temperature a residual tensile strain of ~0.5% persists in all samples independent of thickness. When the films are heated back to the growth temperature of 900 °C, two distinct behaviors are observed: thinner films (~200 nm) follow the thermal expansion of the Si substrate, which results in a tensile strain at the growth temperature. Thicker films (~400 nm) are fully relaxed at 900 °C and thus decoupled from the substrate. These strain behaviors imply that hybrid $ZrB_2$/Si(111) templates are better matched to GaN than any other known substrate. Comparison of the mismatch strains between sapphire, SiC, and bulk $ZrB_2$ substrates with GaN films over a broad temperature range (20–900 °C) illustrates the superior structural and thermal characteristics of hybrid $ZrB_2$/Si(111) templates for nitride integration. Measurements of the $ZrB_2$ dielectric function $\epsilon(\omega)$ and its reflectivity $R(\omega)$ were conducted in the 0.2–7 eV range on thin films and compared for the first time with density functional theory simulations. The dielectric function displays a typical metallic Drude behavior across the wide IR range, with a reflectivity approaching unity at the operational wavelengths of GaN-based intersubband devices. The characteristic Drude plasma energy and lifetimes are compared with those obtained from transport measurements in the isostructural $MgB_2$ analogue. A detailed electronic structure analysis is also used to identify the interband transitions responsible for characteristic features observed at 2.5, 4.3, and 5.7 eV in the spectrum. Collectively our studies pave the way for understanding key optical and thermoelastic design parameters in novel conductive and reflective buffer layers for improved performance in nitride LEDs, fully integrated with silicon.

## 1. Introduction

Transition-metal diborides such as $ZrB_2$, $TaB_2$, and $HfB_2$ are of great interest because they share a layered hexagonal structure with $MgB_2$, the high-temperature superconductor discovered in 2001,[1] and also because their lattice parameters are very close to those of AlN and GaN, which makes them attractive as substrates for the growth of nitride semiconductors.[2] Our prior work in this area has demonstrated proof of principle growth of pure $ZrB_2$ layers and $HfB_2/ZrB_2$ heterostructures on Si(111) and provided a preliminary account of technologically relevant optical and structural properties. Additionally, we have obtained compositional and lattice constant tuning by growth of $Zr_{1-x}Hf_xB_2$ alloy layers directly on Si(111), and this raises opportunities of developing unique nitride device technologies on cheap Si substrates.[3,4]

The design of structures based on boride layers requires a thorough understanding of their thermoelastic behavior, including parameters such as critical thickness and thermal expansion of $ZrB_2$/Si(111) films. Accordingly, we have concentrated our efforts to develop methodologies that lead to routine and reproducible growth of thick $ZrB_2$/Si(111) films (up to 500 nm). These samples were then utilized to determine the temperature dependence of the lattice parameters from ambient up to the growth temperature of 900 °C, which overlaps with the lower range for nitride deposition. In our prior work we examined the dependence of room temperature lattice dimensions on composition for $Hf_xZr_{1-x}B_2$ alloys[4] and found that a constant residual tensile strain remains after cooling from 900 °C. We have also demon-

* To whom correspondence should be addressed.
[†] Department of Chemistry and Biochemistry, Arizona State University.
[‡] Department of Physics, Arizona State University.
[§] Freescale Semiconductor.

(1) Nagamatsu, J.; Nakagawa, N.; Muranaka, T.; Zenitani, Y.; Akimitsu, J. *Nature (London)* **2001**, *410*, 682463.
(2) Kamiyama, S.; Takanami, D.; Tomida, Y.; Iida, K.; Kawashima, T.; Fukui, S.; Iwaya, M.; Kinoshita, H.; Matsuda, T.; Yasuda, T.; Otani, S.; Amano, H.; Akasaki, I. *Phys. Status Solidi A* **2003**, *200*, 67–70.
(3) (a) Hu, C.-H.; Chizmeshya, A. V. G.; Tolle, J.; Kouvetakis, J.; Tsong, I. S. T. *J. Cryst. Growth* **2004**, *267*, 554–563. (b) Tolle, J.; Kouvetakis, J.; Kim, D.-W.; Mahajan, S.; Bell, A.; Ponce, F. A.; Tsong, I. S. T.; Kottke, M. L.; Chen, Z. D. *Appl. Phys. Lett.* **2004**, *84*, 3510–3512.
(4) Roucka, R.; An, Y.-J.; Chizmeshya, A. V. G.; Tolle, J.; Kouvetakis, J.; D'Costa, V. R.; Menendez, J.; Crozier, P. *Appl. Phys. Lett.* **2006**, *89*, 242110.

10.1021/cm702547p CCC: $40.75 
Published on Web 01/05/2008

strated that in the closely related $ZrB_2/HfB_2/Si(111)$ multilayer system a perfect strain equilibration exists between the $ZrB_2$ and $HfB_2$ components of the heterostructure resulting in slightly lower (~+0.3%) strain associated with the smaller bulk lattice constant of $HfB_2$.

Our present work extends this study to the strain behavior as a function of thickness and temperature for single $ZrB_2$/Si(111) layers. An intriguing outcome is that a tensile strain of ~0.5% persists at room temperature in all of our films independent of their thickness. We demonstrate that this strain vanishes at the growth temperature (900 °C) for thick films (400 nm) but that residual strains develop in thin films (200 nm) under the same conditions. The systematic understanding of the structural and thermoelastic behavior developed here enables the use of strain to optimize the design of heteroepitaxial templates, particularly for nitride alloy integration, where the lattice match is already quite favorable.

In addition to these properties, the metallic character of the diborides is technologically attractive, since high thermal conductivity should help reduce the joule heating effect that leads to saturation in the output power of nitride-based light-emitting diodes (LEDs).[5] Recently, high-power (>100 lm/W) vertical LEDs using a metallic alloy substrate were announced by SemiLEDs Corp. Metallic substrates can also act as reflectors that improve the LED performance by increasing the light extraction efficiency. The infrared range below 1.6 eV is particularly important in this respect because nitride semiconductors can be used as quantum well intersubband photodetectors that operate at wavelengths of interest to optical communications.[6]Recently we presented spectroscopic ellipsometry data for $ZrB_2$ films on Si covering the 0.2–8.8 eV energy range.[4] Prior to that work, the only available optical data for this material was the work of Oda and Fukui, covering the 1.4−25 eV energy range,[7] but excluding the relevant low-energy IR range (<1.4 eV). In this paper we present a detailed analysis of the optical properties of $ZrB_2$ as determined from spectroscopic ellipsometry. In particular, our infrared data allow us to determine the range over which the metallic reflectivity approaches unity as well as the dc resistivity that controls Joule heating effects.

## 2. Synthesis

Thick, monocrystalline $ZrB_2$ layers (up to 500 nm thick) were grown on the Si(111) hexagonal surface at optimum temperature, pressure, and reactant concentration of 900 °C, (2–4) × $10^{-6}$ Torr, and ~1% $Zr(BH_4)_4/H_2$, respectively. The reaction mixture based on 4 Torr/L of $Zr(BH_4)_4$ and a large excess of research grade $H_2$ was prepared prior to each deposition by combining the pure compounds in a 1000 mL vacuum flask at total final pressure of 400 Torr. The flask was connected to the gas injection manifold of the deposition chamber, and the manifold was pumped to ~$10^{-8}$ Torr. A boron-doped (1–10 Ω·cm), Si(111) wafer was cleaved to 1 $cm^2$ size substrates to fit the dimensions of the sample stage. Each substrate was sonicated in methanol for 5 min, dried under a stream of purified $N_2$, inserted through a load lock into the growth chamber at a base pressure of 4 × $10^{-10}$ Torr, and heated at 600 °C under UHV to remove surface contaminants until the pressure of the chamber was restored to background levels. The wafer was then subsequently flashed at 1150 °C five times to desorb the native oxide from the surface. To commence film growth, the wafer was heated to 900 °C bypassing direct current though it. The temperature was measured with a single-color pyrometer and allowed to stabilize for 5 min. The precursor mixture was introduced into the chamber at a constant flow rate of ~0.08 sccm, controlled by a manual leak valve. The reaction pressure inside the chamber was maintained at (2–4) × $10^{-6}$ Torr during growth by dynamic pumping using a corrosion-resistant turbomolecular pump. The growth conditions were judiciously tuned in a manner that follows a perfect decomposition mechanism according to the reaction $Zr(BH_4)_4 \rightarrow ZrB_2 + B_2H_6 + 5H_2$. The resulting $ZrB_2$ on Si films grew at a rate of ~1 nm/min, yielding thicknesses up to 500 nm.

The routine deposition of thick $ZrB_2$ films is clearly needed for viable nitride integration. From a synthesis perspective the facile and complete desorption of all diborane byproduct molecules from the surface is therefore a critical requirement for continued crystal growth via layer-by-layer epitaxy to achieve high thicknesses approaching the practical 500 nm level. In this regard the temperature must be sufficiently high (at least 900 °C) to ensure diffusion of the Zr/B adatoms and facilitate assembly of crystalline layers. However, the $B_2H_6$ byproducts are highly reactive at 900 °C and are likely to decompose under these conditions, leading to deposition of elemental boron according to the reaction $B_2H_6 \rightarrow 2B + 3H_2$. This decomposition reaction can be suppressed by introducing a dominant excess of $H_2$ flux which shifts the equilibrium toward $B_2H_6$. It should also be noted that an increase in flux concentration of $Zr(BH_4)_4$ or in reaction temperatures and pressures outside of the optimal range also promotes the decomposition of $B_2H_6$, leading to the immediate contamination of the surface. This terminates the growth, thereby limiting the overall thickness and precluding the use of the resultant material in subsequent applications as templates. Collectively, these constraints lead to a very narrow window of reaction conditions including temperature, pressure, and active reactant flux that ensure systematic and reproducible assembly of smooth crystalline films with thickness approaching micrometers.

## 3. Structural and Morphological Characterization

The resultant films are fully commensurate and perfectly oriented with the underlying hexagonal surface as evidenced by various microstructural and surface characterization techniques including Rutherford backscattering (RBS) ion channeling, atomic force microscopy (AFM) and transmission electron microscopy (XTEM) (see Figure 1). The latter reveals that heteroepitaxy between $ZrB_2(0001)$ and Si(111) is obtained via the coincidence-misfit mechanism in which five lattice rows of Si are aligned with every six rows of

(5) (a) Horng, R. H.; Lee, C. E.; Hsu, S. C.; Huang, S. H.; Wu, C. C.; Kung, C. Y.; Wuu, D. S. *Phys. Status Solidi A* **2004**, *201*, 2786–2790. (b) Uchida, Y; Ito, K.; Tsukimoto, S.; Ikemoto, Y.; Hirata, K.; Shibata, N.; Murakami, M. *J. Electron. Mater.* **2006**, *35*, 1806.
(6) Uchida, H.; Matsui, S.; Holmstr̈; om, P.; Kikuchi, A.; Kishino, K. *IEICE Electron. Express* **2005**, *2*, 566–571.
(7) Oda, S.; Fukui, K. *UVSOR Act. Rep.* **2003**, *2002*, 156.

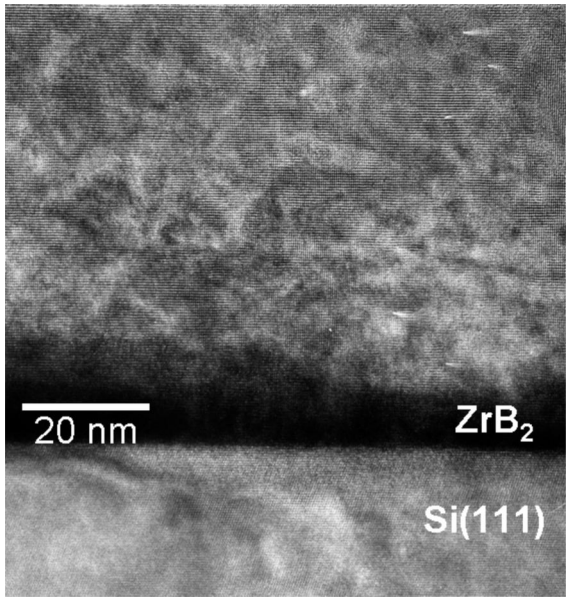


**Figure 1.** Typical high-resolution XTEM micrograph from a thick $ZrB_2$ film showing a representative area of the sample near the epilayer/substrate interface. The data reveal perfect basal plane growth of the hexagonal diboride structure and indicate complete absence of threading dislocations from the film microstructure.

$ZrB_2$, (i.e., "magic mismatch"). This registry results in a periodic array of edge dislocations along the interface which accommodate the large difference in lattice constants.

As mentioned above, it is extremely critical to maintain the optimal growth conditions, and any deviations, however minor, invariably result in either negligible growth of crystalline material or the formation of polycrystalline grains with inferior morphologies. In addition, it is also necessary to cool the samples very slowly from 900 °C to room temperature over the course of 30 min to avoid possible cracking of the layers (depending on thickness) due to the difference in thermal expansion between the $ZrB_2$ material and the Si substrate. The visual appearance of the films is metallic and reminiscent of aluminum mirrors, particularly for samples ~400–500 nm thick. Scanning electron microscopy images of the $ZrB_2$ films in plan view and cross-sectional geometries appeared to be featureless and devoid of fractures or surface cracks. AFM scans showed that the film surface is dominated by an array of shallow undulations with variable lateral extent in the range from 1 to 2 $\mu$m in diameter. Their corresponding heights are found to be dependent on the film thickness and span 2−5 nm for samples with thickness 100−500 nm, respectively. The three-dimensional habit of individual undulations resembles a hexagonal shaped pyramid with a very small aspect ratio. The vertical distance from the base to the apex is ~2–5 nm as determined by AFM measurements (rms roughness). The surface structure suggests that the growth proceeds via formation of large columnar grains which terminate in pyramidal-shaped apexes. The convex surface portion of these features is comprised of stacked hexagonal mesas with progressively decreasing diameters. This morphology is consistent with layer-by-layer growth on the micrometer scale within each grain.

## 4. High-Resolution XRD Film Strain Studies

The structural quality and crystallographic orientation of these thick films were analyzed by high resolution X-ray diffraction (HR-XRD) using a Panalytical X-pert Pro diffractometer. The $\theta-2\theta$ scans revealed only the (001) and (002) peaks of the hexagonal lattice, indicating that the heterostructure is highly oriented and single-crystalline. The double crystal rocking scans of $ZrB_2$ (001) showed full width at half-maxima (fwhm) of 0.15 degrees for 500 nm thick films, indicating no significant tilt between the crystalline domains, consistent with extremely narrow mosaicities within the horizontal direction. For samples with a nominal thickness up to 100 nm a symmetrical envelope of interference fringes is also present in the vicinity of the $ZrB_2$ peak in the $\theta-2\theta$ diffraction patterns. For higher thickness samples these fringes merge within the parent (001) peak.

Extensive off-axis high-resolution measurements were also performed to determine the precise in-plane and vertical lattice parameters and to follow the evolution of the lateral strain as a function of film thickness and temperature. For this purpose, we recorded the ($\bar{1}13$) reciprocal space maps (RSM) of the $ZrB_2$ crystal ($AlB_2$-type structure) owing to its relatively high intensity and geometric accessibility within the scattering configuration of our diffraction apparatus. Routine and reproducible sample alignment was carried out using the (224) reflection of the Si(111) wafer as a reference point due to its close proximity in reciprocal space to the epilayer ($\bar{1}13$) peak. For a typical 500 nm thick $ZrB_2$/Si(111) a detailed analysis of the reciprocal space maps at room temperature yielded correlation lengths of ~0.5 $\mu$m and angular tilt between adjacent grains of ~658 arcseconds, indicating that this material is of high crystalline quality. Similar values are obtained for all films studied irrespective of their thickness. The measured lattice parameters for this sample, $a = 3.1857$ Å and $c = 3.5212$ Å, were found to be slightly different than the *relaxed* bulk $ZrB_2$ values, $a_0 = 3.169$ Å and $c_0 = 3.530$ Å,[8] indicating that the film is tensile strained. As shown below, the strain value obtained from standard elasticity theory is ~0.5%.

The design of template structures based on $ZrB_2$ layers grown on Si requires a thorough understanding of the thickness and temperature dependence of the strain in the system. We begin by determining the variation of the strain as a function of epilayer thickness at room temperature. Accordingly, high-resolution XRD reciprocal space maps of the ($\bar{1}13$) diffraction maxima were measured for a series of films with thicknesses in the range of 50−500 nm. In order to accurately evaluate the in-plane strain of these $ZrB_2$ films, we used the measured $a$ and $c$ lattice constants to calculate the dimensions of the relaxed unit cell for each thickness. For hexagonal films with the [0001] plane oriented normal to the substrate surface, the perpendicular ($\epsilon_c$) and parallel ($\epsilon_a$) strains are given by $\epsilon_c = -2C_{13}\epsilon_a/C_{33}$, where $\epsilon_c = (c - c_0)/c_0$ and $\epsilon_a = (a - a_0)/a_0$. For bulk $ZrB_2$ the known $c/a$ ratio (denoted by $\eta$ below) is 1.1139. The required room temperature elastic constants are $C_{13} = 120.5$ GPa and $C_{33}$

(8) Okamoto, N. L.; Kusakari, M.; Tanaka, K.; Inui, H.; Yamaguchi, M.; Otani, S. *J. Appl. Phys.* **2003**, *93*, 88.

**Table 1. Measured Lattice Parameters *a* and *c* as a Function of Thickness *h* at Room Temperature**

| *h* (nm) | $a_0$ (Å) | $c_0$ (Å) | *a* (Å) (% strain) | *c* (Å) (% strain) |
|---|---|---|---|---|
| 50 | 3.171 | 3.532 | 3.1886 (0.57) | 3.5206 (−0.31) |
| 110 | 3.170 | 3.531 | 3.1862 (0.52) | 3.5208 (−0.29) |
| 150 | 3.170 | 3.531 | 3.1856 (0.51) | 3.5206 (−0.28) |
| 170 | 3.170 | 3.531 | 3.1870 (0.55) | 3.5201 (−0.30) |
| 380 | 3.169 | 3.530 | 3.1849 (0.49) | 3.5209 (−0.27) |
| 400 | 3.169 | 3.530 | 3.1858 (0.52) | 3.5201 (−0.29) |
| 500 | 3.170 | 3.531 | 3.1857 (0.50) | 3.5212 (−0.28) |

[a] The corresponding lattice parameters $a_0$ and $c_0$ were calculated using $\eta = 1.1139$ and the observed[8] value $\zeta = -0.553$, yielding the strain values listed in parentheses.

$= 436.1$ GPa,[8] yielding $\zeta = -2C_{13}/C_{33} = -0.553$. From inversion of the strain relation the relaxed lattice constants are then given by $a_0 = \{c/\eta - \zeta a\}/\{1-\zeta\}$ and $c_0 = \eta a_0$, and these are listed in Table 1 together with the experimental values. To derive the relaxed lattice parameters $a_0$ and $c_0$ of our 50–500 nm thick $ZrB_2$ layers, we make the very reasonable approximation that $\eta$ for the *relaxed* epitaxial film is identical to that of the equilibrium bulk crystals. This allows us to compute the strains states of the films as given in parentheses next to the measured *a* and *c* values in Table 1.

We note that the relaxed lattice constants of all the films are calculated to be virtually the same using our procedure and match the known values for the bulk phase $a_0 = 3.169$ Å and $c_0 = 3.530$ Å. This finding demonstrates the remarkable consistency of the in-plane strain determination and shows that the lattice parameters are accurate to ~0.001 Å. This strain analysis also shows that all $ZrB_2$ films with thicknesses larger than 50 nm exhibit a tensile strain with average value of $\epsilon_a \sim +0.51\%$ and $\epsilon_c \sim -0.30\%$ and that this tensile strain does not change with increasing thickness up to 500 nm at room temperature. These residual strains were found to be remarkably robust even after the films were heated either via rapid thermal annealing for several seconds up to 1100 °C or by postgrowth treatments under UHV conditions for up to 24 h at 900 °C.

The fact that all of the $ZrB_2$ films considered were found to be tensile strained has significant implications for the use of these materials as buffer layers for nitride integration with Si. The average measured value of *a* at room temperature is essentially identical to that of GaN ($a = 3.189$ Å), indicating that these buffers might even be more suitable platforms for integration of nitrides on Si than previously described. However, for this strategy to succeed, a thorough understanding of the evolution of strain in the $ZrB_2$ films with temperature is also required. The need for such a study is underscored by the following observation: if we assume that the $ZrB_2$ films are relaxed at the growth temperature of 900 °C and track the Si substrate (expand at the same rate) when cooling from the growth temperature, we can use the measured coefficients of thermal expansion (CTE) for bulk $ZrB_2$ ($\alpha_a$ for the basal dimension) and bulk Si ($\alpha$) to predict the strain at room temperature. Using $\alpha_a = 6.66 \times 10^{-6}\ K^{-1}$ [8] for $ZrB_2$ and $\alpha = 3.78 \times 10^{-6}\ K^{-1}$ for Si; however, we predict a strain $\epsilon_a(20\ °C) \sim 0.2\%$, which is much smaller than the ~0.5% values observed in our samples (Table 1). In the context of this discrepancy our $ZrB_2$/Si(111) epitaxial system appears to exhibit a different behavior in comparison to typical compliant film systems grown epitaxially on mismatched substrates, i.e., Ge grown on Si. One distinction in our system, which may account for the higher than expected tensile strain (~0.5%) and its thickness independence at room temperature, is that the stiffness of the $ZrB_2$ epilayer is much greater than that of the Si substrate. Furthermore, at the high growth temperatures in our study (900 °C) the silicon substrate becomes far less mechanically rigid. The large differences in the elastic and thermal properties of $ZrB_2$ and Si are therefore likely to produce complicated and perhaps unexpected strain response in the heterostructure, particularly since the synthesis involves large variations in temperature (e.g., $\Delta T \sim 900$ °C, compared to $\Delta T \sim 400$ °C in conventional semiconductor applications).

To elucidate the origin of this residual strain, we next undertook a study of the thermal behavior using representative $ZrB_2$/Si samples with thicknesses of 200 and 400 nm, intermediate among those shown in Table 1. If the room-temperature strain in these samples is controlled by the thermal expansion differential between the $ZrB_2$ and Si upon cooling, then the above discussion implies that there must be a nonvanishing strain at the growth temperature. This strain would likely be associated with the registry at the interface (coincidence of 6 $ZrB_2$ with 5 Si lattice rows[3]) established within the first few nanometers of growth and would become immutably fixed no matter how thickly the film is subsequently grown. On the other hand, for sufficiently thick films we might expect a vanishing strain (full relaxation) at the growth temperature. In this study we demonstrate that both mechanisms are in operation.

We begin by analyzing the thinner (200 nm) sample, which we heated to a series of temperatures in the range 20–900 °C. The corresponding lattice parameters were recorded at each temperature using the diffractometer's Anton Paar high-temperature stage capable of reaching 900 °C. The heating was conducted under inert atmosphere conditions in a dynamic flow of UHP nitrogen at a 4 psi overpressure to avoid oxidation of the samples. At each temperature the film was realigned using the Si (224) reflection to correct for any sample drift associated with the diffractometer stage expansion. The lattice parameters of the boride film were determined from measurements of the off-axis $ZrB_2$ ($\bar{1}13$) reciprocal space maps (RSM). A representative RSM map for the 200 nm thick film is shown in Figure 2.

Table 2 lists the temperature dependence of the observed film lattice parameters, *a* and *c* for $ZrB_2$, the corresponding lattice constant *a* for Si, the calculated relaxed values $a_0(T)$ and $c_0(T)$, and the associated strains $\epsilon_{||}(T)$ and $\epsilon_{\perp}(T)$ obtained from our analysis. The latter were obtained using the same formalism as described above in the context of the thickness dependence of the film strain. In addition, we assume that the *c*/*a* ratio, $\eta(T)$, of a fully relaxed $ZrB_2$ film is the same as that of a corresponding equilibrium bulk $ZrB_2$ crystal *at any given temperature*. The variation of $\eta(T)$ with temperature was obtained from the recently measured CTE for bulk $ZrB_2$ (including the temperature dependence of the CTE itself).[8] The temperature dependence of the elastic ratio, $\zeta(T) = -2C_{13}(T)/C_{33}(T)$, was also obtained from recent measurements of the elastic constants $C_{13}(T)$ and $C_{33}(T)$ for bulk $ZrB_2$ crystals,[8] and our analysis assumes that the strain

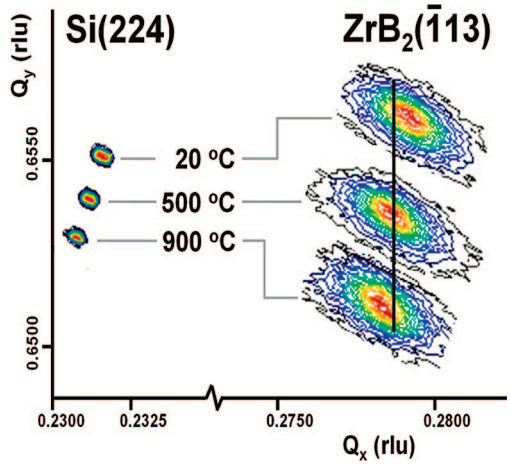


**Figure 2.** Temperature dependence of the Si(224) and $ZrB_2$(113) diffraction peaks of a 200 nm thick $ZrB_2$ film grown on Si(111). The data indicate that the in-plane lattice constants of the film expand slightly from 20 to 900 °C (the line is a vertical reference which shows the relative displacement of the ($\bar{1}$13) peaks) while the corresponding vertical dimension undergoes a much larger expansion. The substrate lattice constant shows the expected isotropic expansion behavior over the same temperature range.

relation $\epsilon_\perp(T) = \zeta(T)\epsilon_{||}(T)$ remains valid over the temperature range of our study (20–900 °C).

Table 2 also lists the coincidence lattice misfit $F$ introduced by Matthews,[9] which in our case is defined as $F = (5d_{Si-Si} - 6a_{ZrB_2})/(6a_{ZrB_2})$, where $d_{Si-Si} = a_{Si}/\sqrt{2}$ is the Si−Si distance in the (111) plane. We denote by $F_0$ the coincidence misfit calculated with bulk $ZrB_2$ parameters. From our definition it is clear that $F + \epsilon_a = F_0$. This bulk coincidence misfit $F_0$ was calculated using thermal expansion data from ref 8 and has a room temperature value of 0.983%, which means that the $ZrB_2$ basal lattice parameter is slightly less than required for a perfect 6/5 coincidence. At the growth temperature of 900 °C the misfit decreases to a value of 0.733%, since the CTE of Si is smaller than that of the basal plane of $ZrB_2$. At this temperature the basal plain strain is $\epsilon_a = 0.26\%$, which means that about 35% of the coincidence misfit is taken up by tensile strain in the $ZrB_2$ film. The remaining 65% is thus accommodated by additional misfit dislocations or by straining the interfacial region. Upon cooling to room temperature the coincidence misfit remains essentially constant, indicating that the rate of contraction of the $ZrB_2$ film in the basal plane matches that of the underlying Si. This tracking behavior can be clearly seen in the temperature dependence of the strain in the 200 nm thick film which is presented graphically in Figure 3. The lines represent the predicted trend assuming measured strains at the growth temperature and a $ZrB_2$ $a$-axis thermal expansion equal to that of the underlying Si. The agreement is excellent, confirming that the higher than expected tensile strain observed at room temperature (~0.5%) is due to a tensile strain $\epsilon_a = 0.26\%$ already present at the growth temperature. This, combined with the observation that all samples produced in our thickness dependence study (Table 1), has approximately the same value of tensile strain (0.5%) at room temperature and suggests that all films should also have the same value of strain ~0.26% at the growth temperature. However, this appears to contradict the very plausible expectation that the strain in the thick bulklike $ZrB_2$ films must also eventually vanish with increasing thickness.

To further elucidate the strain status of $ZrB_2$ films as a function of thickness both at their growth temperature and upon cooling, and resolve the above issues, we repeated the 200 nm film temperature study for a thicker 400 nm sample. The results are shown in Table 3 and also graphically in Figure 4. Note that while a residual strain of ~+0.26% was observed in the basal plane in the 200 nm film at the growth temperature of 900 °C, the corresponding strain essentially vanishes in the 400 nm film described in Table 3. Figure 4 compares the observed data (symbols) with the predicted trend (lines) assuming zero strain at the growth temperature and a $ZrB_2$ $a$-axis thermal expansion equal to that of the underlying Si for the 400 nm thick sample. The comparison shows that the strain in both $a$ and $c$ is larger than expected, which indicates that the $ZrB_2$ is not thermally pinned to the underlying Si. Note that in the case of the 200 nm thick film (see Figure 3) the temperature dependence of the strain followed this model precisely, indicating that the epilayer and Si expand at the same rate. Thus, the most significant distinction between the thermal behavior of the thin and thick $ZrB_2$ films is that thin 200 nm sample tracks the Si but the 400 nm thick sample does not. This in turn implies the existence of a "pseudo-critical" thickness in the range of 200–400 nm, at the growth temperature 900 °C.

To verify that these puzzling results are not due to phase inhomogeneities in the thick film samples or to measurement errors, we show in Figure 5 the measured $a$ and $c$ parameters for the 400 nm film, the calculated relaxed values $a_0$ and $c_0$, and we also include, as solid lines, the lattice parameters for bulk $ZrB_2$ as a function of temperature. As in the case of the 200 nm sample, the agreement between the relaxed parameters for our sample and the bulk values is excellent, confirming that the thermal behavior of our film should be understandable in terms of the elastic properties of standard $ZrB_2$ crystals.

The observation of virtually no strain at the growth temperature suggests a bulk-like behavior for thicker samples. However, if the 400 nm film was behaving in a bulklike fashion, its thermal expansion as it cools should be closer to that of bulk $ZrB_2$, but the opposite is observed: whereas for bulk $ZrB_2$ there is a $\Delta a/a = 0.58\%$ contraction between 900 and 20 °C, the contraction is 0.40% for the 200 nm film and only 0.14% for the 400 nm film. An examination of the temperature dependence of the coincidence misfit provides some insight into the behavior of the thick film: at the growth temperature, the film is essentially relaxed, even at the expense of a larger coincidence misfit $F$ than in the 200 nm sample. However, it appears that upon cooling the film takes up strain as a way to minimize the coincidence misfit. Eventually, at room temperature, the coincidence misfit has been reduced to the same value as in the 200 nm film.

We believe that the above observations cannot be explained in terms of a strain energy equilibration model that includes only the Si substrate and the $ZrB_2$ film. Even if we

(9) (a) Matthews, J. W. Report No. RC 4266 No. 19084, **1973**. (b) Vook, R. W. *Int. Met. Rev.* **1982**, *27*, 209–245. (c) Ploog, K. H.; Trampert, A. *Cryst. Res. Technol.* **2000**, *35*, 793–806.

**Table 2. Thermal Analysis of the 200 nm Thick $ZrB_2$ Film on Si(111)**

| $T$ (°C) | $a$ (Si) | $a^{FIT}$ (Si) | $\zeta$ (T) | $\eta$ (T) | $a_0$ (Å) | $c_0$ (Å) | $a$ (Å) (% strain) | $c$ (Å) (% s train) | $F$ (%) (film) | $F_0$ (%) (bulk) |
|---|---|---|---|---|---|---|---|---|---|---|
| 20 | **5.4308** | 5.4308 | −0.553 | 1.11392 | 3.1690 | 3.5300 | **3.1835** (0.46) | **3.5212** (−0.25) | 0.525 | 0.983 |
| 200 | **5.4339** | 5.4343 | −0.557 | 1.11400 | 3.1728 | 3.5345 | **3.1876** (0.47) | **3.5253** (−0.26) | 0.450 | 0.933 |
| 500 | **5.4404** | 5.4404 | −0.566 | 1.11413 | 3.1796 | 3.5425 | **3.1922** (0.40) | **3.5346** (−0.22) | 0.425 | 0.850 |
| 700 | **5.4449** | 5.4445 | −0.572 | 1.11422 | 3.1838 | 3.5475 | **3.1942** (0.33) | **3.5408** (−0.19) | 0.442 | 0.792 |
| 900 | **5.4506** | 5.4486 | −0.578 | 1.11431 | 3.1883 | 3.5527 | **3.1965** (0.26) | **3.5474** (−0.15) | 0.475 | 0.733 |

[a] Measured values of $a$ and $c$ for $ZrB_2$ and $a$(Si) are listed in bold font. The relaxed lattice constants, $a_0$ and $c_0$, at each temperature were obtained from a strain analysis using the known temperature dependence of bulk $ZrB_2$ elastic constants and that of the equilibrium bulk $c/a$ ratios (as described in the text). Also listed is the temperature dependence of the Si lattice constant which is well-described by a constant linear CTE $3.78 \times 10^{-6}$ $K^{-1}$ over the range 20–900 °C. The last two columns list the temperature dependence of the coincidence misfit parameter. This quantity vanishes if the lattice parameters of the film and the substrate are in a perfect 6/5 ratio.

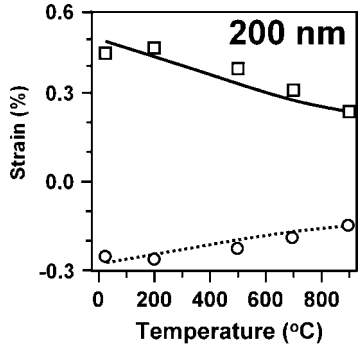


**Figure 3.** Measured $a$-axis (squares) and $c$-axis (circles) strain as a function of temperature for the 200 nm thick $ZrB_2$ film. The solid and dotted lines represent the predicted in-plane and vertical strains, respectively, calculated by assuming measured strains at the growth temperature and a $ZrB_2$ $a$-axis thermal expansion equal to that of the underlying Si.

were to assume that additional misfit dislocations relax the growth-temperature strain in the 400 nm film, such an assumption would not lead to a simple explanation of the temperature dependence of its lattice parameters. It appears that any convincing explanation must allow for the possibility that a thin interfacial layer with its own elastic properties and strain status plays a role in the energy minimization. We note that the initial nucleation of $ZrB_2$ on Si(111) is known to involve a $\sqrt{3} \times \sqrt{3}$ Si surface reconstruction with B atoms in a subsurface layer, and the growth proceeds through the "6/5" coincidence mechanism ("magic" mismatch) described above.[3] Clearly, the atomic structure of the interfacial layer is very different from crystalline Si and $ZrB_2$, and therefore it cannot be modeled in terms of bulk material properties. The different behaviors of the 200 and 400 nm films, as well as the observation that all films have the same room temperature strain, regardless of thickness, are likely to require an interfacial layer with strongly anharmonic elastic properties in which the elastic constants are temperature-dependent and perhaps even vary nonlinearly. Experimentally, the atomic positions in the nanometer-size interfacial region cannot be determined from our HR-XRD measurements. However, we note that significant strain fields running into the silicon are clearly visible in HR XTEM micrographs obtained from these samples. In fact, a common problem that we have encountered in the preparation of thin specimens for cross-sectional TEM examination is the delamination of the thick film from the substrate, which is presumably caused by the large strains in the silicon within the interface region.

A schematic illustration of the strain distributions in the thin and thick $ZrB_2$ films *at the 900 °C growth temperature*, including the interfacial layer, is shown in Figure 6. Note that in the case of the thick, relaxed film the $ZrB_2$ applies a larger compressive stress on the interfacial layer, as shown by the "fade to black" contrast at the $ZrB_2$−Si interface in the right panel. The minimization of this stress may be the reason for the larger than expected room temperature strain in the thick film, as indicated above. From a microstructural perspective the strain mismatch is accommodated by a fixed number of edge dislocations at the interface, consistent with the ∼6/5 coincidence, which "pin" the epilayer to the substrate to partially relieve the large misfit strain between the two materials. Thus, the strains in $ZrB_2$ are determined by the thin initiation layer in the early stages of film growth (at 900 °C), and this layer then serves as a robust template for subsequent film growth. Because of the high mechanical stiffness of the $ZrB_2$ lattice, the registry adopted by this initial layer subsequently determines the strain state of the rest of the $ZrB_2$ film at the growth temperature. In this study we have shown that this strain depends on thickness and that once a zero strain state is obtained there is in principle no upper limit to the thickness that can be achieved on Si.

The thermal strain behavior observed in our $ZrB_2$ films has significant implications for the use of these materials as buffer layers for nitride integration with Si. The temperature dependences of the mismatch strains between GaN and typical candidate substrates, including sapphire, SiC, and bulk $ZrB_2$, are compared with $ZrB_2$/Si(111) in the inset of Figure 7. As shown here, both sapphire and SiC exhibit constant mismatch strain over the entire temperature range (note the logarithmic scale). This is due to the large difference in lattice parameters between these substrates and GaN. For bulk $ZrB_2$, however, a systematic and significant decrease in mismatch strain is observed with increasing temperature. This indicates that although there is better lattice matching between bulk $ZrB_2$ and GaN relative to SiC and $Al_2O_3$, the nearly 10-fold thermal variation of mismatched strain in the former could lead to cracking or other structural degradation in devices. By contrast, the hybrid substrate based on 200 nm thick $ZrB_2$ film grown on Si(111) possesses the smallest mismatch strain, which vanishes at ∼400 °C and actually becomes negative at high temperatures (see main panel of Figure 7). To our knowledge, this system represents the first "zero mismatch" template for GaN integration, exhibiting the smallest absolute value of strain over the entire temperature among the substrates considered. For the 400 nm thick film the strain is also very small relative to the other candidate substrates and exhibits essentially *no temperature dependence* (see

**Table 3. Thermal Analysis of the 400 nm Thick $ZrB_2$ Film on Si(111) Showing the Same Parameters as in Table 2[a]**

| $T$ (°C) | $a$(Si) | $a^{FIT}$(Si) | $\zeta$(T) | $\eta$(T) | $a_0$ (Å) | $c_0$ (Å) | $a$ (Å) (% strain) | $c$ (Å) (% strain) | $F$ (%) (film) | $F_0$ (%) (bulk) |
|---|---|---|---|---|---|---|---|---|---|---|
| 20 | **5.4307** | 5.4307 | −0.553 | 1.11392 | 3.1692 | 3.5302 | **3.1843** (0.48) | **3.5209** (−0.26) | **0.491** | **0.983** |
| 200 | **5.4338** | 5.4343 | −0.557 | 1.11397 | 3.1729 | 3.5345 | **3.1850** (0.38) | **3.5270** (−0.21) | **0.533** | **0.933** |
| 400 | **5.4378** | 5.4384 | −0.563 | 1.11403 | 3.1779 | 3.5403 | **3.1859** (0.25) | **3.5353** (−0.14) | **0.575** | **0.875** |
| 600 | **5.4422** | 5.4425 | −0.569 | 1.11409 | 3.1816 | 3.5445 | **3.1868** (0.16) | **3.5412** (−0.09) | **0.625** | **0.812** |
| 800 | **5.4466** | 5.4466 | −0.575 | 1.11415 | 3.1857 | 3.5493 | **3.1879** (0.07) | **3.5479** (−0.04) | **0.675** | **0.758** |
| 900 | **5.4488** | 5.4486 | −0.578 | 1.11418 | 3.1877 | 3.5517 | **3.1887** (0.03) | **3.5511** (−0.02) | **0.691** | **0.733** |

[a] Note that small residual strain essentially vanishes at the growth temperature of 900 °C, in contrast with the residual strain of 0.26% found for the 200 nm sample (Table 2).

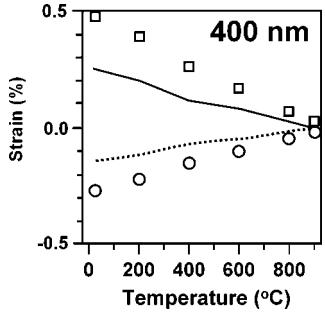


**Figure 4.** Measured *a*-axis (squares) and *c*-axis (circles) strain as a function of temperature for the 400 nm thick $ZrB_2$ film. The solid and dotted lines represent the predicted in-plane and vertical strains, respectively, assuming measured strains at the growth temperature and a $ZrB_2$ *a*-axis thermal expansion equal to that of the underlying Si. Note the larger than expected strains upon cooling in both *a*- and *c*-axes, indicating that the epilayer does not track Si.

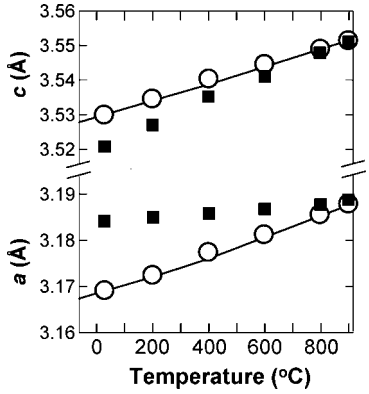


**Figure 5.** Temperature dependence of the measured *a*- and *c*-axis lattice parameters of the $ZrB_2$ film (solid squares), their calculated relaxed values (open circles), and the corresponding measured bulk data obtained from ref 8 (solid lines). Note that our relaxed values very closely match those of the bulk material.

Figure 7), indicating that this GaN/$ZrB_2$/Si(111) heterostructure based on thick $ZrB_2$ templates would experience the smallest degree of thermal stress. Overall, these data demonstrate the superiority of our buffer approach for practical integration of nitrides with silicon on both structural and thermoelastic grounds.

## 5. Optical Properties

Our prior work on films of $ZrB_2$ and $Zr_{1-x}Hf_xB_2$ provided a preliminary experimental and theoretical account of novel optical properties and highlighted the potential of these systems as structurally and optically tunable reflective buffer layer systems with applications in optoelectronics.[4] Here we provide a more detailed account of both the measurement and theoretical simulation of the $ZrB_2$ dielectric function $\epsilon(\omega)$ and its reflectivity $R(\omega)$ in the energy range from ~0.2–7 eV. Our aim is to identify the origin of various characteristic spectral features in the reflectivity plot from the 1–7 eV range and elucidate the low-energy (<1 eV) infrared properties, which are related to $ZrB_2$ metallic behavior.

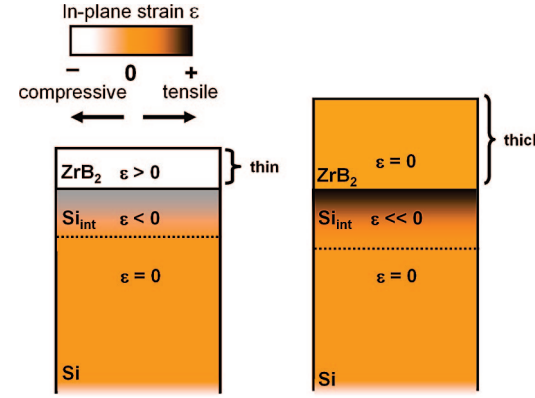


**Figure 6.** Schematic representation of the strain distribution in the thin and thick $ZrB_2$/Si heterostructures at the growth temperature of 900 °C.

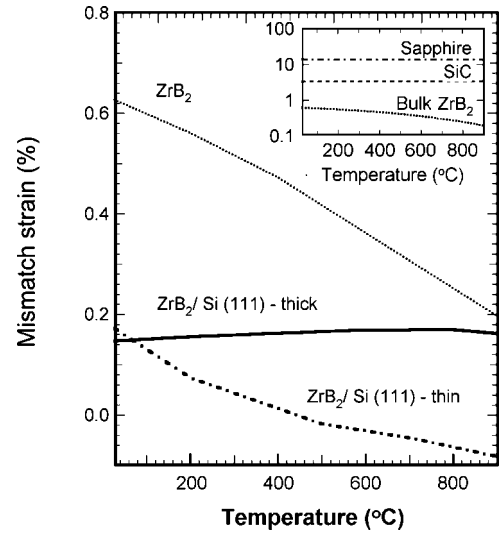


**Figure 7.** Comparison of the temperature dependence of the mismatch strains of GaN with $ZrB_2$/Si(111) films and bulk $ZrB_2$ substrates, illustrating the superior matching characteristics of the $ZrB_2$/Si(111) system. Inset shows corresponding behavior on sapphire, SiC, and bulk $ZrB_2$ substrates.

**5.1. Electronic Structure Calculations.** State-of-the-art density functional theory calculations of the electronic structure were carried out using the full-potential linearized augmented plane wave method (FPLAPW), as implemented in the EXCITING code.[10] We employ the Perdew–Zunger parametrization of the exchange-correlation potential and energy density of the

(10) Dewhurst, J. K.; Sharma, S.; Ambrosch-Draxl, C. EXCITING code, http://exciting.sourceforge.net/.

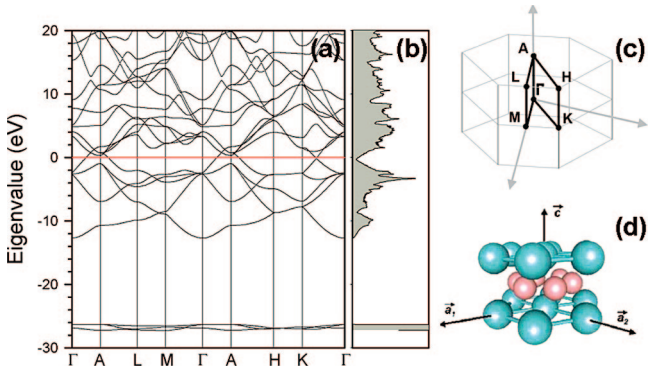


**Figure 8.** (a) Electronic band structure of $ZrB_2$; red horizontal line denotes the Fermi level. The compact manifold of states just below −26 eV is due to Zr p-states. (b) Density of states indicating semimetallic character, (c) "roadmap" of the Brillouin zone used in the band structure plot, and (d) crystal structure of $ZrB_2$ (Zr atoms blue, B atoms pink).

Ceperley−Alder electron gas functional.[11,12] At room temperature $ZrB_2$ crystallizes in the $AlB_2$-type structure (space group *P6/mmm*) with lattice constants $a = 3.186$ Å and $c = 3.521$ Å and atomic positions (in lattice coordinates) Zr: (000), B: ($^1/_3{}^2/_3{}^1/_2$), ($^2/_3{}^1/_3{}^1/_2$). Static lattice optimization of the cell parameters at the LDA level using the FPLAPW method corroborates this equilibrium structure but yields slightly contracted lattice constants ($a = 3.145$ Å, $c = 3.487$ Å) corresponding to an underestimate of 3.5% in the volume per formula unit. Part of this discrepancy is associated with the neglect of zero-point energy and vibrational entropy effects, which are beyond the scope of the present study. To ensure meaningful comparisons between the measured and simulated optical properties, we therefore carried out all of our simulation studies at the room temperature experimental structure of $ZrB_2$.

Well-converged self-consistent ground-state solutions of the Kohn–Sham equations were obtained in the FPLAPW basis using $R_{MT}K_{MAX} = 7$ (product of the atomic sphere radii and the interstitial plane-wave cutoff), a maximum $G$ vector ($G_{MAX}$) of 12.0 in the expansion of the interstitial density and potential, and an angular momentum cutoff of $l_{MAX} = 10$ for the corresponding density and potential within the atomic spheres, whose radii were set to 2.0 and 1.45 au for Zr and B, respectively. Brillouin zone integration were carried out using the tetrahedron method on a 12 × 12 × 12 Γ-centered grid, corresponding to 133 $k$-points in the irreducible wedge.

The band structure of $ZrB_2$ and the corresponding total density of states (DOS) are shown in Figure 8. The figure also contains a schematic of the unit cell structure and a sketch of the Brillouin zone and high symmetry path used to plot the band dispersion. Perhaps the most distinctive feature of the electronic structure is the "pseudogap", which appears as a valley in the DOS around the position of the Fermi level ($E_F$). Besides conferring semimetallic properties to $ZrB_2$, it has been suggested that the relatively low DOS near $E_F$ leads to weak electron–phonon coupling in this binary compound. The species and angular momentum decompositions of the DOS (partial DOS) are shown in Figure 9, which indicate that the valence band structure is of a mixed hybrid nature devolving primarily from an admixture of B p-states and Zr d-states. The lowest-lying bands in this energy range are largely boron s-like and account for the ~4 eV wide feature near −10 eV. The DOS in the conduction band is dominated by contributions from the Zr d-states up to 10 eV above $E_F$, while boron p-states account for the features at higher energies, as shown in the figure.

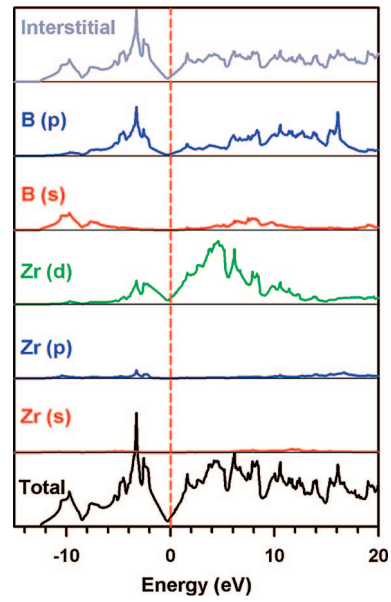


**Figure 9.** Decomposition of the density of states by site (Zr, B) and by angular momentum character. The topmost panel is a plot of the interstitial contribution.

All of the simulated optical properties described in the present work are obtained from the complex dielectric function $\epsilon(\omega) = \epsilon_1(\omega) + i\epsilon_2(\omega)$. In the case of semimetallic $ZrB_2$ both interband and intraband transitions contribute to the dielectric response, with the latter dominating at low energies. Three particle interactions between electrons, photons, and phonons can also in principle produce indirect interband and intraband electronic transitions. While the incorporation of these effects is beyond the scope of the present work, it is believed that they essentially contribute a smooth background to the spectral response.[13] In our work we therefore only explicitly include direct interband and intraband transitions. The interband component of the imaginary part $\epsilon_2(\omega)$ of the dielectric function is obtained within the random phase approximation (RPA) as[14]

$$\epsilon_2(\omega) = \frac{\hbar^2 e^2}{\pi m^2 \omega^2} \sum_{n,m} \int d\mathbf{k} |p_{n,m,\mathbf{k}}|^2 [f(E_{n,\mathbf{k}}) - f(E_{m,\mathbf{k}})] \delta(E_n(\mathbf{k}) - E_m(\mathbf{k}) - \hbar\omega) \quad (1)$$

where $p_{n,m,\mathbf{k}}$ are the momentum matrix element for the transition from bands $n$ and $m$ at wave vector $\mathbf{k}$, with corresponding band energies $E_n(\mathbf{k})$ and $E_m(\mathbf{k})$, and $f(E)$ are occupation numbers. The real part $\epsilon_1(\omega)$ is then obtained from a Kramers–Kronig integration:

(11) Perdew, J. P.; Zunger, A. *Phys. Rev. B* **1981**, *23*, 5048.
(12) Ceperley, D. M.; Alder, B. J. *Phys. Rev. Lett.* **1980**, *45*, 566.
(13) Smith, N. V. *Phys. Rev. B* **1971**, *3*, 1862.
(14) Landau, L. D.; Lifshitz, E. M. *Electrodynamics in Continuous Media*; Pergamon: Oxford, 1960.

$$\epsilon_1(\omega) = 1 + \frac{2}{\pi} P \int_0^\infty d\omega' \frac{\omega' \epsilon_2(\omega')}{(\omega'^2 - \omega^2)} \quad (2)$$

To model the contribution from direct intraband transitions, we follow our previous work[4] and adopt the Drude expression $\epsilon^{\text{Drude}}(\omega) = 1 - \omega_p^2/(\omega^2 + i\omega\Gamma)$, where $\Gamma$ is the lifetime broadening (we use $\Gamma \sim 0.11$ eV, which corresponds to a relaxation time of $\sim$7 fs; see below) and $\omega_p$ is the free-electron plasma frequency, given by the expression[14]

$$\omega_p^2 = \frac{\hbar^2 e^2}{\pi m^2} \sum_n \int d\mathbf{k} \, |p_{n,n,\mathbf{k}}|^2 \delta(E_{n,\mathbf{k}} - E) \quad (3)$$

For binary crystals with hexagonal symmetry, like $ZrB_2$, the optical response is in general anisotropic with two independent components for $\epsilon(\omega)$ and $\omega_p$ corresponding to electric field polarizations $\boldsymbol{E}\|c$ and $\boldsymbol{E}\perp c$. These are obtained by evaluating the matrix elements appearing in eqs 1−3 using appropriate momentum operator components.

It should be noted that a very dense $40 \times 40 \times 40$ $k$-point mesh (3234 irreducible $k$-points) was required to converge the linear optical properties, including the plasma frequency. We also significantly increased the number of empty states in the optics calculations to capture higher energy transitions that may be involved in the optical spectrum. As an example, using the latter grid we obtain $\omega_p^{xx} = 4.29$ eV and $\omega_p^{zz} = 4.06$ eV for the plasma frequencies in basal plane and parallel to the $c$-axis and an isotropic average value of 4.21 eV. This is smaller than our earlier reported value 4.56 eV, which was obtained using a coarser grid of 2130 $k$-points. Once convergence is achieved, the normal incident reflectivity for both polarizations is calculated from the dielectric functions defined above using the Fresnel equation

$$R = \frac{(n-1)^2 + k^2}{(n+1)^2 + k^2} \quad (4)$$

where $n$ and $k$ are the real and imaginary part of the complex refractive index defined by $n + ik = \sqrt{\epsilon}$. The isotropic values of the dielectric functions, plasma frequencies, and reflectivities (see below) are then obtained taking an average according to $\langle N \rangle = {}^1/_3(2N_a + N_c)$, where $N_a$ and $N_c$ are quantities corresponding to the basal plane and $c$-axis, respectively.

**5.2. Optical Properties from Ellipsometry.** Spectroscopic ellipsometry measurements were carried out at room temperature using a variable-angle spectroscopic ellipsometer[15] with a computer-controlled compensator and an infrared variable-angle spectroscopic ellipsometer (IR-VASE) with a rotating compensator. This system is based on a Fourier-transform infrared spectrometer. Both instruments are manufactured by J.A. Woollam Co. We studied in detail two $ZrB_2$ samples with different thickness ($\sim$50 and 150 nm). Using the vis−UV instrument, the dielectric function of the films was determined from 0.74 to 6.6 eV with 0.03 eV steps. Two angles of incidence (70° and 80°) were used. Infrared measurements at an angle of incidence of 60° were carried out for the 150 nm sample. These measurements covered the 0.03 to 0.83 eV range.

The $ZrB_2$ films were modeled as a three-layer system consisting of a Si substrate, a film layer, and a surface layer. Since $ZrB_2$ is optically absorbing, there is a strong correlation between thickness of the film and optical constants.[16] In order to extract reliable optical data, we modeled the surface layer as a thin film consisting of 50% $ZrB_2$ and 50% voids in the Bruggeman approximation.[17] The thicknesses of the surface films were taken as twice the surface roughness rms value, as obtained from the AFM measurements, and were kept fixed in the fitting process. The thicknesses of the $ZrB_2$ films were taken as equal to the thickness determined from the RBS measurements minus the AFM roughness rms value, and they were also kept fixed. Finally, the optical constants for the Si substrate were taken from the literature.[15] These assumptions fix all parameters of the optical model except for the optical constants of $ZrB_2$, which are then obtained from a point-by-point fit as described in ref 18. Our model assumes an isotropic dielectric function tensor, which is not required by symmetry in $ZrB_2$ but is justified as a good approximation by the theoretical simulations described above which predict that the anisotropy in the reflectivity is essentially zero over most of the energy range considered, with a maximum deviation of <10%. The self-consistency of the fit was first verified by keeping the point-by-point optical constants fixed, while allowing the thicknesses of the two top layers (diboride and surface) to vary. The fit then converges, as expected, to the same values of thicknesses for surface layer and film layer that were assumed on the basis of AFM and RBS data. We also verified that the optical constants obtained from the two samples were virtually the same. Since the films thicknesses are very different, this lends further support to the reliability of the fits. The maximum deviation between the two samples for the real part of the refraction index is $\Delta n = 0.2$ in the UV, while for the imaginary part the deviation is $\Delta k < 0.1$. The reflectivity of the two samples obtained using the above procedure is virtually identical. Finally, the Kramers–Kronig consistency of the optical constants was confirmed by verifying that the point-by-point fit dielectric function can be accurately described with an optical dispersion model consisting of Gaussian oscillators.

The real and imaginary parts of the complex dielectric function in the infrared are shown in Figure 10. As can be seen from this figure, the dielectric function displays the typical metallic Drude behavior in the infrared. The data are fit with an expression of the form

$$\epsilon(\omega) = 1 + \epsilon^{\text{Drude}}(\omega) + \epsilon^{\text{inter}}(\omega) \quad (5)$$

Here $\epsilon^{\text{inter}}(\omega)$ corresponds to interband transitions, which are modeled as Gaussian oscillators, and the Drude term is given in terms of the plasma frequency $\omega_p$ and the relaxation time $\tau$ (or, alternatively, in terms of the dc resistivity $\rho_{dc}\tau$) as

(15) Herzinger, C. M.; Johs, B.; McGahan, W. A.; Woollam, J. A.; Paulson, W. *J. Appl. Phys.* **1998**, *83*, 3323–3336.

(16) McGahan, W. A.; Johs, B.; Woollam, J. A. *Thin Solid Films* **1993**, *234*, 443.

(17) Bohren, C. F.; Huffman, D. R. *Absorption and Scattering of Light by Small Particles*; Wiley-Interscience: New York, 1983; p 530.

$$\epsilon^{\text{Drude}}(\omega) = -\frac{{\omega_p}^2}{\omega^2 + i\omega/\tau} = -\frac{4\pi}{\rho_{dc}(\omega^2\tau + i\omega)} \quad (6)$$

The plasma frequency can be expressed as ${\omega_p}^2 = 4\pi ne^2/m_{opt}$, where $n$ is the conduction electron density and $m_{opt}$ is the average optical mass. The fit parameters are $\hbar\omega_p = 4.22$ eV and $\tau = 9.0$ fs. Note that (perhaps coincidentally) this value of the plasma energy is in excellent agreement with our FPLAPW-LDA prediction of 4.21 eV. From these parameters we find $\rho_{dc} = 30.6\ \mu\Omega\cdot$cm. Transport measurements in single $ZrB_2$ crystals yield a room temperature resistivity $\rho_{dc}(300\text{ K}) = 6\text{–}10\ \mu\Omega\cdot$cm, which implies $\tau \sim$ 30–45 fs, and a residual low-temperature resistivity $\tau_0 =$ 0.5–2 $\mu\Omega\cdot$cm (refs 19 and 20). A comparative analysis of the film and bulk results in the spirit of Matthiesen's rule suggests for our film samples a residual low-temperature resistivity $\rho_0 = 21\text{–}25\ \mu\Omega\cdot$cm, about 1 order of magnitude higher than in bulk single crystals. We emphasize, however, that we are comparing optical data from films with transport measurements in bulk crystals. Discrepancies have been noted between transport and optical measurements of the dc resistivity in systems with an optical response characterized by more than one Drude term.[18] The $ZrB_2$ material could be such an example, since it has a complex conduction band structure with several charge pockets at the Fermi level.[21] We have verified that our data are very well fit with a single Drude term (the parameters of the Drude expression in eq 6 remain stable if the fit is limited to a very narrow low-frequency range), but the presence of an additional Drude term that might become apparent at extremely low frequencies (beyond the reach of our ellipsometer) cannot be ruled out. Ellipsometric measurements on bulk $ZrB_2$ single crystals should shed light on possible discrepancies between transport and optical data in this system.

If we tentatively assume that the optically derived resistivity can be compared with transport data, a possible reason for the higher resistivity of our material is its thin film nature. In fact, a similar effect is observed in the isostructural $MgB_2$ compound, for which the residual resistivity in 400 nm thick films grown on sapphire substrates is 5 times larger than in single-crystal $MgB_2$.[22] We note that the residual resistivity in bulk $ZrB_2$ crystals is very low compared to $MgB_2$,[23] which magnifies the relative contribution of possible film defects. The only defects that we have observed in our $ZrB_2$ films are the strain relieving edge dislocations located at the interface. Threading analogues typically observed in mismatched heteroepitaxy are not present in our case. On the other hand, interface roughness scattering is known to make a significant contribution whenever the film thickness $d$ is much less than the carrier mean free path $l$.[24] Using de Haas–van Alphen data for $ZrB_2$,[20] we estimate a Fermi velocity $v_F = 1.2 \times 10^8$ cm/s, which at room temperature leads to $l \sim 50$ nm in the bulk material. Thus roughness scattering at the Si/$ZrB_2$ interface is not expected to be the main reason for the increased resistivity in our $d = 150$ nm film. Similarly, the XRD discussion above suggests grain sizes of at least 500 nm, so that grain boundary scattering is not likely to play a dominant role either. Thus, more research is needed to clarify the origin of the higher residual resistivity of our $ZrB_2$ films, including, as emphasized above, infrared experiments in bulk $ZrB_2$ single crystals.

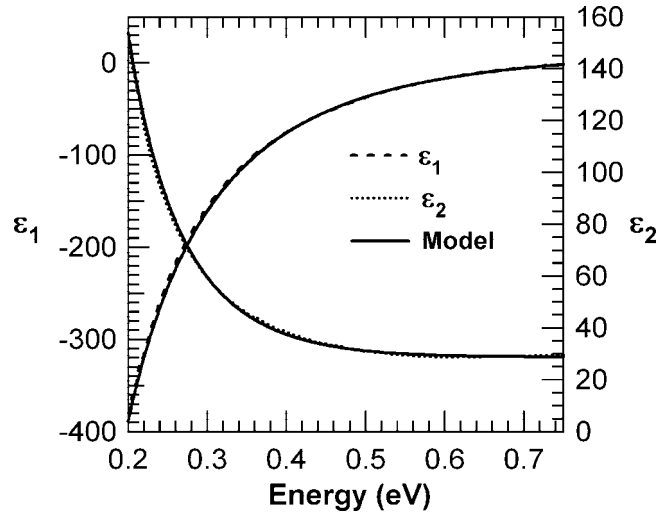


**Figure 10.** Real ($\epsilon_1$) and imaginary ($\epsilon_2$) parts of the infrared complex dielectric function of $ZrB_2$ films grown on Si(111). The dielectric function is obtained from a point-by-point fit of the ellipsometric data, as described in the text. The model solid line is a fit with eqs 5 and 6.

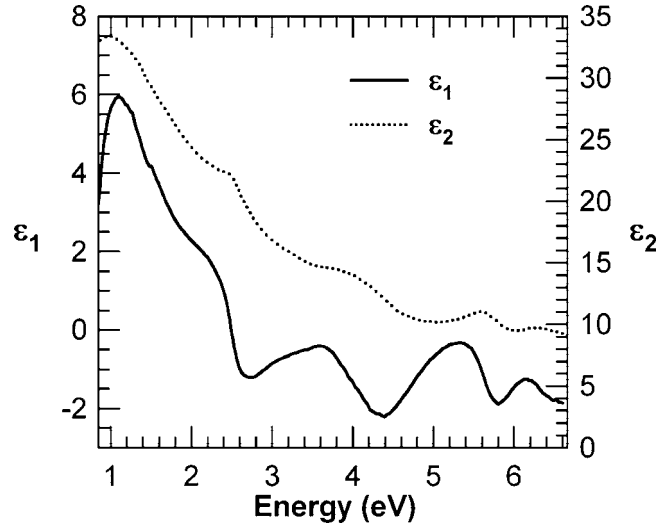


**Figure 11.** Real ($\epsilon_1$) and imaginary ($\epsilon_2$) parts of the vis–UV complex dielectric function of $ZrB_2$ films grown on Si(111). The dielectric function is obtained from a point-by-point fit of the ellipsometric data, as described in the text.

The real and imaginary parts of the dielectric function from the near-IR to the UV are shown in Figure 11, and the corresponding air reflectivity (including the Drude region)

(18) Perucchi, A.; Caimi, G.; Ott, H. R.; Degiorgi, L.; Bianchi, A. D.; Fisk, Z. *Phys. Rev. Lett.* **2004**, *92*, 067401.
(19) Gasparov, V. A.; Sidorov, N. S.; Zver'kova, I. I. *Phys. Rev. B* **2006**, *73*, 094510.
(20) Forzani, E.; Winzer, K. *Eur. Phys. J. B* **2006**, *51*, 29.
(21) (a) Ihara, H.; Hirabayashi, M.; Nakagawa, H. *Phys. Rev. B* **1977**, *16*, 726. (b) Rosner, H.; An, J. M.; Pickett, W. E.; Drechsler, S. L. *Phys. Rev. B* **2002**, *66*, 024521.
(22) (a) Kim, H.-J.; Kang, W. N.; Choi, E.-M.; Kim, M.-S.; Kim, K. H. P.; Lee, S.-I. *Phys. Rev. Lett.* **2001**, *87*, 087002. (b) Masui, T.; Yoshida, K.; Lee, S.; Yamamoto, A.; Tajima, S. *Phys. Rev. B* **2002**, *65*, 214513.
(23) Yanson, I. K.; Naidyuk, Yu G.; Kvitnitskaya, O. E. *Mod. Phys. Lett. B* **2003**, *17*, 657.
(24) Fishman, G.; Calecki, D. *Phys. Rev. Lett.* **1989**, *62*, 1302.

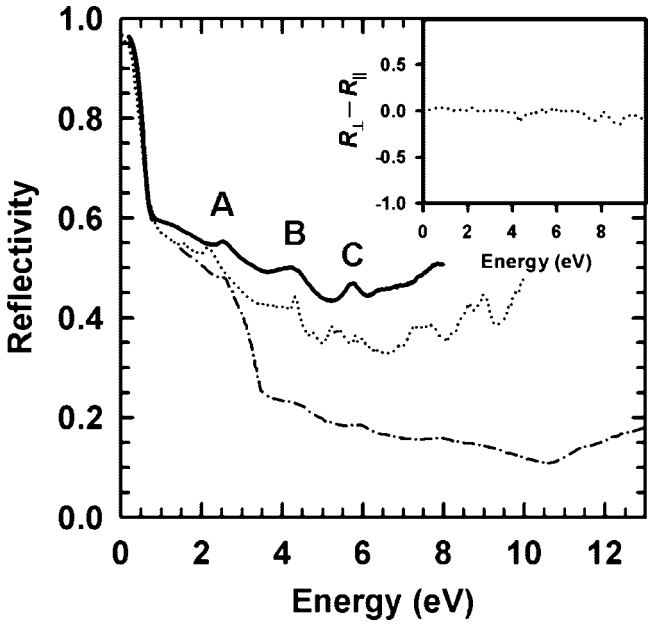


**Figure 12.** Solid line: optical reflectivity of $ZrB_2$ films grown on Si(111), calculated from the dielectric function data in Figures 10 and 11. Dotted line: all-electron FPLAPW-DFT simulations. Dot-dashed line: reflectivity data from bulk $ZrB_2$ crystals as obtained by Oda and Fukui. The inset is anisotropy in the reflectivity based on theory ($R_\parallel$ and $R_\perp$ are the reflectivities with polarization parallel and perpendicular to the basal plane, respectively).

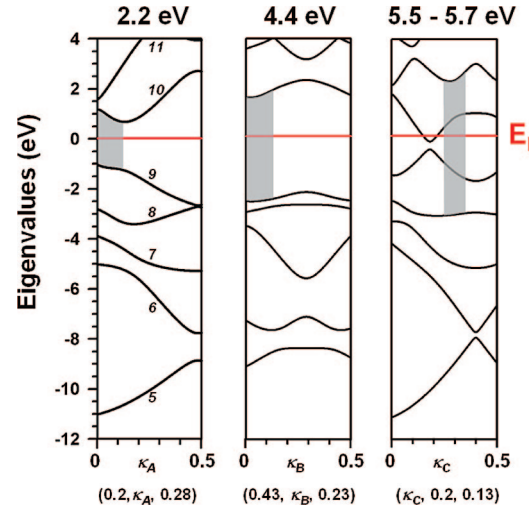


**Figure 13.** Band diagrams illustrating the electronic origin of the spectral features found in the reflectivity at 2.2, 4.4, and 5.5 eV. The shaded regions indicate interband transitions, and location in $k$-space, for which the momentum matrix element contributions to the spectral features are largest.

is shown in Figure 12. As mentioned above, the only available optical data for $ZrB_2$ prior to this paper was the work of Oda and Fukui covering the 1.4−25 eV energy range,[7] which is also plotted in Figure 12 and compared with our data. A reasonable agreement is seen in the region below 3 eV, but at higher energies there is a rather abrupt drop in reflectivity in Oda and Fukui's data that is found in neither our experimental nor simulated data (Figure 12, solid and dotted line, respectively). On the other hand, both our and Oda and Fukui's data sets agree well on the energy of the three features at 2.6, 4.3, and 5.7 eV, which are related to interband transitions. Note that the values of the vis/UV reflectivity shown here are slightly higher than those reported in our earlier work (ref 4). The reason for the discrepancy is that the thicknesses of the surface layer and the $ZrB_2$ film were allowed to vary in the fitting process in ref 4, whereas here we have chosen to use the RBS and AFM values, as discussed above. We have found that this latter approach produces more consistent results when a common model is sought to fit ellipsometric measurements of $ZrB_2$ and $Hf_xZr_{1-x}B_2$ alloys. Our results for the alloys will be published elsewhere. The discrepancy between the two fitting procedures for $ZrB_2$ provides an estimate of the error in the ellipsometric determination of the dielectric function. However, neither the infrared reflectivity nor the energy of the vis/UV interband features is affected by the choice of fitting procedure.

Figure 12 also compares the observed reflectivity with our LDA simulations. The dotted line represents the isotropic average reflectivity, while the inset is a plot of the anisotropy calculated as the difference between the reflectivity corresponding to an $E$-field perpendicular and parallel to the $ZrB_2$ $c$-axis, respectively. Our simulations predict that the reflectivity is essentially, isotropic ($R_\perp - R_\parallel \sim 0$) over most of the energy range from 0 to 10 eV but that significant deviations on the order of 5–10% are expected near 4.4 and 9.5 eV. As can be seen from the comparison, the theoretical reflectivity reproduces the experimental data fairly well, including the positions of the main experimental spectral features labeled A (2.6 eV), B (4.3 eV), and C (5.7 eV) in the figure. The corresponding values from simulation are 2.2, 4.4, and 5.5–5.7 eV, respectively. We note that for energies <1 eV our simulated results slightly underestimate the observed reflectivity using our calculated value of $\hbar\omega_p = 4.21$ eV and a best fit value of $\tau = 7$ fs. The slightly lower value for the lifetime obtained here is likely associated with the differences between the calculated and measured interband component to the reflectivity, which is nonempirical in the former case. The very good agreement between theory and experiment in the low-energy range indicates that the single oscillator assumption used in the experimental fitting is a good approximation.

To fully elucidate the origin of the observed spectral features labeled A, B, and C in Figure 12, we carried out a detailed analysis of the electronic band structure. By systematically sorting the momentum matrix elements corresponding to interband transitions (see eq 1) according to both energy and $k$-point index, we identified band combinations with dominant spectral weight for each of the three features. According to our simulations, these transitions do not occur at high-symmetry points in reciprocal space, but rather from narrow regions within the Brillouin zone as described by the segments below each panel corresponding to each feature in Figure 13. Here the values of the parameters $\kappa_A$, $\kappa_B$, and $\kappa_C$ are given in terms of lattice coordinates in $k$-space: $\mathbf{k}_1 = 2\pi/[(a\sqrt{3})/2](1,0,0)$, $\mathbf{k}_2 = 2\pi/[(a\sqrt{3})/2](^1/_2,^{\sqrt{3}}/_2,0)$, and $\mathbf{k}_3 = (2\pi/c)(0,0,1)$. From these plots it is evident that features A and B at 2.2 and 4.4 eV, respectively, involve transitions from band 9 to band 10 while feature C in the vicinity of 5.5–5.7 eV involves direct interband transitions from band 8 to band 11 (see numbering

in the band structure of first panel, Figure 13). The gray areas shown in Figure 13 denote the approximate range corresponding to the largest momentum matrix elements.

## 6. Concluding Remarks

We have presented a comprehensive experimental study of the structural, thermoelastic, and optical behavior of $ZrB_2$ films grown on silicon. Films ranging in thickness from 50 to 500 nm possessing device quality morphological and structural properties were systematically grown on Si(111) and fully characterized using RBS ion channeling, AFM, and XTEM. High-resolution XRD was used to analyze the thickness and temperature dependence of the films' strain state, and detailed comparisons were made with the corresponding bulk $ZrB_2$ thermal behavior for the first time. At room temperature all $ZrB_2$ films grown on silicon displayed a residual tensile strain of $\sim$0.5% independent of their thickness. However, detailed structure analysis carried out near the growth temperature of 900 °C revealed that the strain could be completely relaxed by increasing the thickness of the films to achieve bulklike $ZrB_2$ behavior. To elucidate the mechanism responsible for the thickness-independent 0.5% strain found at room temperature, we carried out a comparative temperature-dependent strain study from 20 to 900 °C for representative thick (400 nm) and thin (200 nm) films. The main finding is that the thinner sample tracks the Si (expands at the same rate) but that thicker sample does not. This implies the existence of a "pseudo-critical" thickness within the range 200–400 nm *at the growth temperature 900 °C*. In the case of the thicker film our analysis suggests that the large interface strains induced upon cooling are partially absorbed by a thin, structurally altered silicon layer near the $ZrB_2$/Si interface, which effectively decouples the thermal behavior of the film from the underlying substrate. A comparison of the mismatch strains between sapphire, SiC, and bulk $ZrB_2$ substrates and GaN films over a broad temperature range (20–900 °C) indicates that our $ZrB_2$/Si(111) templates possess superior structural and thermal characteristics for nitride integration. Furthermore, the larger-than-expected strains result in an essentially perfect basal-plane lattice matching between $ZrB_2$ buffers and GaN films.

The fundamental optical properties of the $ZrB_2$ buffers are also of great technological interest in view of their novel semimetallic character. However, potential application of $ZrB_2$ thin films in the context of both structural/thermal integration *and* reflective behavior requires a deeper understanding of their fundamental electronic behavior. We therefore carried out the first complementary experimental and theoretical studies of the thin film $ZrB_2$ dielectric function $\epsilon(\omega)$ and its reflectivity $R(\omega)$ in the 0.2–7 eV range. In the infrared regime we found that the energy dependence of the dielectric function is essentially captured by a single-term metallic Drude description. At higher energies (2–7 eV) we observe a number of spectral features related to interband transitions, which are also exhibited by bulk $ZrB_2$. Electronic structure calculations based on all-electron density functional theory (FPLAPW) at the LDA level were used to calculate the band structure, density of states, dielectric function, and reflectivity of $ZrB_2$. From an analysis of these calculations the interband transitions responsible for the spectral features at 2.5, 4.3, and 5.7 eV in the experimental reflectivity were identified for the first time. Our simulations also predict a weak anisotropy in the optical reflectivity in the vicinity of 4–5 and 8–9 eV, with isotropic behavior throughout the rest of the energy range.

**Acknowledgment.** This work was supported by the Science Foundation of Arizona and the National Science Foundation (EEC - 0438400). Computational studies were performed using the resources of the Fulton High Performance Computing Initiative at Arizona State University.

CM702547P